

# New constraints on the molecular gas content of a $z \sim 8$ galaxy from JVLA CO(J=2-1) observations

Gareth C. Jones<sup>1\*</sup>, Joris Witstok<sup>2,3</sup>, Alice Concas<sup>4</sup>, Nicolas Laporte<sup>2,3</sup>

<sup>1</sup>*Department of Physics, University of Oxford, Denys Wilkinson Building, Keble Road, Oxford OX1 3RH, UK*

<sup>2</sup>*Kavli Institute for Cosmology, University of Cambridge, Madingley Road, Cambridge CB3 0HA, UK*

<sup>3</sup>*Cavendish Laboratory, University of Cambridge, 19 JJ Thomson Avenue, Cambridge CB3 0HE, UK*

<sup>4</sup>*European Southern Observatory, Karl-Schwarzschild-Strasse 2, D-85748 Garching bei München, Germany*

Received X / Accepted Y

## ABSTRACT

As the primary fuel for star formation, molecular gas plays a key role in galaxy evolution. A number of techniques have been used for deriving the mass of molecular reservoirs in the early Universe (e.g., [CII]158  $\mu\text{m}$ , [CI], dust continuum), but the standard approach of CO-based estimates has been limited to a small number of galaxies due to the intrinsic faintness of the line. We present Jansky Very Large Array (JVLA) observations of the  $z \sim 8.31$  galaxy MACS0416\_Y1, targeting CO(2-1) and rest-frame radio continuum emission, which result in upper limits on both quantities. Adding our continuum limit to the published far-infrared (FIR) spectral energy distribution (SED), we find a small non-thermal contribution to the FIR emission, a low dust mass ( $\log_{10}(M_{\text{D}}/M_{\odot}) \sim 5$ ), and an abnormally high dust temperature ( $T_{\text{D}} \gtrsim 90$  K) that may indicate a recent starburst. Assuming a low metallicity ( $Z/Z_{\odot} \sim 0.25$ ), we find evidence for  $M_{\text{H}_2, \text{CO}} \lesssim 10^{10} M_{\odot}$ , in agreement with previous [CII] investigations ( $M_{\text{H}_2, [\text{CII}]} \sim 10^{9.6} M_{\odot}$ ). Upcoming JWST observations of this source will result in a precise determination of  $Z$ , enabling better constraints and an unprecedented view of the gaseous reservoir in this primordial starburst galaxy.

**Key words:** galaxies: high-redshift - galaxies: ISM - radio continuum: galaxies

## 1 INTRODUCTION

Molecular gas reservoirs in galaxies act as potential fuel for future star formation. This gas may be accreted from cosmic filaments or through collisions with gas-rich companions (i.e., ‘wet’ mergers). Recent observations suggest that the cosmic density of molecular gas increased from early times until a peak between  $z \sim 3$  and  $z \sim 1$  and decreased to the present day (e.g., Decarli et al. 2019; Aravena et al. 2023; Boogaard et al. 2023). This evolution matches the cosmic density of star formation rate (e.g., Bouwens et al. 2020), suggesting that star formation in early galaxies ( $z > 4$ , or  $\lesssim 1.5$  Gyr after the Big Bang) was powered by gas accreted from past mergers and inflows.

Since  $\text{H}_2$  lacks a permanent dipole moment, molecular gas is difficult to observe directly. Instead, we must rely on indirect tracers. The most commonly used tracer has been carbon monoxide (CO), which is the second most abundant molecule ( $N_{\text{CO}}/N_{\text{H}_2} \sim 10^{-4}$ ) and features a host of rotational emission lines (i.e.,  $J \rightarrow J - 1$ ; see review of Bolatto et al. 2013). By observing CO(1-0), the molecular gas mass of a galaxy may be found by assuming a mass-to-light ratio (i.e.,  $M_{\text{H}_2} = \alpha_{\text{CO}} L'_{\text{CO}(1-0)}$ ). This ratio  $\alpha_{\text{CO}}$  has standard values for starburst ( $\sim 0.8 M_{\odot} (\text{K km s}^{-1} \text{pc}^2)^{-1}$ ) and Milky Way-like systems ( $\sim 4.36 M_{\odot} (\text{K km s}^{-1} \text{pc}^2)^{-1}$ ), as well as metallicity-dependent forms (e.g., Narayanan et al. 2012). While other tracers based on line emission (e.g. [CI], [CII], HD; Walter et al. 2011; Zanella et al. 2018; Jones et al. 2020), dust continuum emission

(e.g., Decarli et al. 2022; Eales et al. 2023; Hashimoto et al. 2023), and dust attenuation (e.g. Güver & Özel 2009; Brinchmann et al. 2013; Concas & Popesso 2019) have risen to wide use, CO still acts as the gold standard molecular gas mass estimator.

Due to its faintness with respect to [CII], detection of CO at  $z > 4$  requires long exposure times and/or exceptionally bright targets. Despite this, there have been a multitude of CO detections between  $4 < z < 6$  in bright starburst galaxies (e.g., Hodge et al. 2012; Jiménez-Andrade et al. 2018; Pavesi et al. 2018; Riechers et al. 2021a,b; Zavala 2021; Vieira et al. 2022; Eales et al. 2023; Frias Castillo et al. 2023; Stanley et al. 2023), quasar hosts (e.g., Riechers et al. 2006), and normal star-forming galaxies (SFGs; e.g., D’Odorico et al. 2018; Pavesi et al. 2019; García-Vergara et al. 2022; Lee et al. 2023). Studies of CO within the epoch of reionisation (EoR;  $z \gtrsim 6$ ) have been more limited, with CO detections in bright galaxies up to  $z \sim 7.5$  (e.g., Jarugula et al. 2021; Ono et al. 2022; Decarli et al. 2022, 2023; Feruglio et al. 2023). In this work, we detail the results of some of the first observations of CO at  $z > 8$ , targeting the  $z \sim 8.31$  galaxy MACS0416\_Y1.

MACS0416\_Y1 was originally selected as a  $z > 8$  Lyman break candidate behind the lensing cluster MACS0416 (Laporte et al. 2015). This source is gravitationally lensed by the cluster, resulting in a magnification of  $\mu \sim 1.43$  (Kawamata et al. 2016)<sup>1</sup>. It has been detected in continuum emission using multiple Hubble Space Telescope (HST) Wide Field Camera 3 (WFC3) filters (e.g., F125W,

\* E-mail: gareth.jones@physics.ox.ac.uk

<sup>1</sup> We will assume this factor throughout this work.

F140W, F160W), the Ks band of the Very Large Telescope (VLT) High Acuity Wide field K-band Imager (HAWK-I), channel 2 of the Spitzer Infrared Array Camera (IRAC), and the Atacama Large Millimetre/submillimetre Array (ALMA)  $850\mu\text{m}$  (Laporte et al. 2015; Brammer et al. 2016; Tamura et al. 2019).

It features both strong [CII]  $158\mu\text{m}$  ( $L_{[\text{CII}]} = (1.40 \pm 0.22) \times 10^8 L_{\odot}$ , Bakx et al. 2020) and [OIII]  $88\mu\text{m}$  ( $L_{[\text{OIII}]} = (13 \pm 3) \times 10^8 L_{\odot}$ ; Tamura et al. 2019) emission, implying a star formation rate  $\text{SFR} \sim 60 M_{\odot} \text{ year}^{-1}$ . By combining a ultraviolet to far-infrared (UV-FIR) spectral energy distribution (SED) model and a stellar evolution model, Tamura et al. (2019) estimate  $M_{H_2} \sim 10^{10} M_{\odot}$  and  $M_{*} \sim 10^{9.5} M_{\odot}$ . Using the star-forming main sequence (MS) formulations derived from observations of  $0 < z < 6$  galaxies (e.g., Speagle et al. 2014; Popesso et al. 2023), an MS galaxy with this stellar mass at this redshift is expected to feature a  $\text{SFR} \sim 25 M_{\odot} \text{ year}^{-1}$  (in agreement with the  $5 < z < 10$  results from simulations; e.g., D’Silva et al. 2023). Because MACS0416\_Y1 features a higher SFR, it is likely a starburst galaxy. A low-resolution observation of the [CII] velocity field shows evidence for a rotational gradient (Bakx et al. 2020), which is resolved into three star-forming clumps with a beam-deconvolved spatial extent of  $0.5'' \times 0.3''$  in high-resolution [OIII] observations (Tamura et al. 2023) that are also seen in rest-frame UV photometry.

Using the Jansky Very Large Array (JVLA), we observed this object in CO(2-1) emission and rest-frame radio continuum emission. While this resulted in a non-detection, it enables us to place new constraints on the molecular gas content, non-thermal emission, and dust properties in this high-redshift source. We use a standard concordance cosmology ( $h_0, \Omega_m, \Omega_{\Lambda} = 0.7, 0.3, 0.7$ ) throughout, where  $1'' \sim 4.7 \text{ kpc}$  at  $z \sim 8.31$ .

## 2 DATA CALIBRATION AND IMAGING

Our observations were taken with the JVLA in A-configuration over nine 3 hr executions between 24 December 2020 - 29 January 2021 under the partially completed project 20B-194. The bandpass and flux calibrator was 3C147, while J0416-1851 was used as a phase calibrator. In order to target CO(2-1) at 24.758 GHz, we used two basebands in K-band (20.488-21.512 GHz and 24.488-25.512 GHz), each with eight spectral windows (SPWs) of 64 channels of 2 MHz.

Due to an error in scan intent declarations, the flux and bandpass calibration scans were unusable, so an extra 30 minute scan of the phase calibrator was taken. Since J0416-1851 is a high-quality (‘P’-grade) calibrator, we were able to use these observations to determine its flux and thus use it as a flux/bandpass calibrator for the previous scans.

The nine executions were calibrated using the Common Astronomy Software Applications package (CASA; CASA Team et al. 2022) using a standard high-frequency calibration pipeline, but with a manual flux calibration (i.e., no CASA fluxscale) due to the observation setup. The resulting visibilities were inspected, and additional flagging of bad antennas and edge flagging was performed before the pipeline was re-run. One execution was excluded because of significant calibration issues.

Continuum images were created using CASA tclean with the line-free SPWs of all acceptable executions in multifrequency synthesis (MFS) mode with natural weighting. This results in a synthesised beam of  $0.19'' \times 0.09''$  at  $180.0^{\circ}$  and root mean square (RMS) noise level of  $1.9 \mu\text{Jy beam}^{-1}$ .

The basebands of each execution that contained redshifted CO(2-1) emission were separated (CASA split), combined into a single

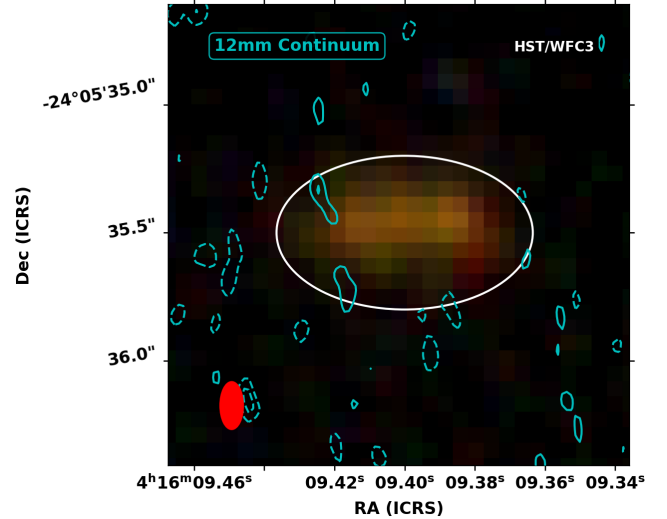


**Figure 1.** Continuum emission ( $\nu_{obs} = 25 \text{ GHz}$ ) of MACS0416\_Y1 (cyan contours), where contours are shown at  $\pm 2, 3, 4, \dots \times \sigma$  ( $1\sigma = 1.9 \mu\text{Jy beam}^{-1}$ ). For reference, we include a three-colour image of HST/WFC3 (F105W/F125W/F140W). The synthesised beam is represented by a filled red ellipse to the lower left, while the assumed aperture of MACS0416\_Y1 is given as a hollow white ellipse.

measurement set (CASA concat), and imaged (CASA tclean in ‘cube’ mode, natural weighting, 6 MHz channels), resulting in a cube with a mean synthesised beam of  $0.17'' \times 0.09''$  at  $180.1^{\circ}$  and a mean RMS noise level per channel of  $\sim 30 \mu\text{Jy beam}^{-1}$ . Since no continuum emission is detected (see Section 3.1), we do not perform continuum subtraction.

## 3 ANALYSIS

### 3.1 Continuum

No significant emission is detected in our continuum image ( $\nu_{obs} \sim 25 \text{ GHz}$ ), as seen in Figure 1. To place a conservative estimate on the continuum emission, we use a large elliptical aperture of double the deconvolved [OIII] $88\mu\text{m}$  full width at half maximum (FWHM) of Tamura et al. (2019), resulting in  $1.0'' \times 0.6''$ . This implies a  $3\sigma$  upper limit of  $S_{12mm} < 28 \mu\text{Jy}$ . Here, we combine this upper limit with archival continuum flux density values to examine the constraints on dust properties and SFR that these implies.

Only three FIR continuum observations have been published to date:  $S_{850\mu\text{m}} = 137 \pm 26 \mu\text{Jy}$  and  $S_{1.5\text{mm}} < 18 \mu\text{Jy}$  from Tamura et al. (2019), and  $S_{1.14\text{mm}} < 174 \mu\text{Jy}$  from Bakx et al. (2020), where each limit is  $3\sigma$ . Several other ALMA programs have targeted the  $850\mu\text{m}$  and  $1.14 \text{ mm}$  emission, so future works may combine them to place tighter estimates on each flux density. However, only one program has targeted this source at  $\sim 3.2 \text{ mm}$  (band 3, 2021.1.00075.S; PI Ono). We apply the ALMA staff calibration (i.e., ScriptForPI.py) to the raw data and create a  $3.2 \text{ mm}$  continuum image using CASA tclean with MFS mode, natural weighting, and a conservative frequency range to exclude possible line emission. This results in a continuum non-detection, and a  $3\sigma$  upper limit of  $S_{3.2\text{mm}} < 21 \mu\text{Jy}$ .

We begin by adopting the modified blackbody (MBB) model of Carniani et al. (2019), which includes the cosmic microwave background (CMB) corrections of da Cunha et al. (2013) and makes no assumption on optical depth. If we assume the dust is emitted from

approximately the same area as the [OIII] emission and adopt a dust absorption coefficient of  $\kappa_o = 0.04 \text{ m}^2 \text{ kg}^{-1}$  at a critical density of 250 GHz (Beelen et al. 2006), then this model is reduced to three free parameters: the dust mass ( $M_D$ ), dust temperature ( $T_D$ ), and dust emissivity index ( $\beta_{IR}$ ). To extend this model to lower frequencies, we include the non-thermal emission (i.e., combined synchrotron and free-free) model of Algera et al. (2021), which also only has three free variables: the synchrotron slope ( $\alpha_{NT}$ ), a normalisation factor ( $S_{\nu'}$ ), and the fraction of flux from the free-free component ( $f_{th}$ ).

With only one detection and four upper limits, we cannot place constraints on all six free parameters of this model simultaneously. Instead, we may explore the constraints that our radio and FIR points give. First, we assume standard values for  $\alpha_{NT} = 0.8$  and  $f_{th} = 0.1$  (e.g., Condon 1992; Algera et al. 2021), and normalise the non-thermal emission so that our continuum limits are met (see ‘MaxR’ results in left panel of Figure 2). This results in a limit of  $S_{1.4\text{GHz}} < 120 \mu\text{Jy}$ , or a  $\text{SFR}_{1.4\text{GHz}}$  limit of  $\lesssim 2.5 \times 10^4 M_\odot \text{ year}^{-1}$  (Condon 1992). This is much greater than the expected SFR of this object ( $\text{SFR} \sim 60 - 100 M_\odot \text{ year}^{-1}$ ; Bakx et al. 2020), so this limit is not highly constraining. Since the radio continuum point is not informative, we may assume a smaller  $\text{SFR} \sim 10^2 M_\odot \text{ year}^{-1}$ , which implies a much smaller radio contribution (see ‘MinR’ results in right panel of Fig. 2).

In both cases of radio emission (‘MaxR’ and ‘MinR’), we examine the FIR portion of the SED by assuming a dust temperature (40 K, 85 K, or 130 K) and explore what  $M_D$  and  $\beta_{IR}$  values are required for a given dust temperature to satisfy the  $S_{850\mu\text{m}}$  detection and  $S_{1.5\text{mm}}$  non-detection. We find that a larger non-thermal contribution requires a smaller dust mass and steeper spectrum (i.e., higher  $\beta_{IR}$ ). On the other hand, a higher dust temperature requires a larger dust mass and shallower slope, and results in a higher FIR luminosity (area between the dashed vertical lines) and thus  $\text{SFR}_{FIR}$ .

Since this SED only contains a single point, these models are for illustration only. But given the SFR of this source and the fact that  $\beta_{IR}$  values greater than  $\sim 2.5$  are rarely seen (e.g., Witstok et al. 2023), it is likely that: i.) Non-thermal emission does not significantly contribute to the FIR luminosity, ii.) The dust temperature is high ( $\geq 90$  K), and iii.) The dust mass is quite small ( $M_D \sim 10^5 M_\odot$ ). These last two conclusions are in agreement with the SED analysis of Bakx et al. (2020).

Note that these dust masses are smaller than that of Tamura et al. (2019,  $M_D = 4 \times 10^6 M_\odot$ ), who assumed  $\beta_{IR} = 1.5$ ,  $T_D = 50$  K, and a different dust absorption coefficient. The primary difference is their use of a UV-to-FIR SED model that includes dust attenuation and scaled FIR templates, rather than our use of a single MBB with a flexible  $\beta_{IR}$  and  $T_D = 50$  K. We are unable to recreate a model that uses  $\beta_{IR} = 1.5$  and  $T_D = 50$  K and obeys  $S_{850\mu\text{m}} = 137 \pm 26 \mu\text{Jy}$  and  $S_{1.5\text{mm}} < 18 \mu\text{Jy}$ , suggesting that a future flexible UV-to-FIR SED model is required.

Briefly, we note that the derived luminosity-weighted dust temperature limit implied by our exploration ( $T_D \geq 90$  K) is much higher than commonly used mass-weighted dust temperatures at low-redshift ( $T_D = 25$  K; Scoville et al. 2016), as well as other high-redshift luminosity-weighted values (e.g.;  $T_D \sim 40 - 70$  K at  $z \sim 5 - 7$ , Bakx et al. 2021; Ikarashi et al. 2022; Jarugula et al. 2021; Manning et al. 2022; Vieira et al. 2022). While dust temperature has been found to increase with redshift (e.g., Bouwens et al. 2020; Witstok et al. 2023; Jones & Stanway 2023), most correlations would predict  $T_D \sim 60 - 70$  K at  $z = 8.31$ . The fact that we predict a higher temperature could be interpreted in multiple ways: i.) MACS0416\_Y1 may contain abnormally warm dust due to its high specific SFR (e.g., Liang et al. 2019; Mitsuhashi et al. 2023),

ii.) The correlation between redshift and dust temperature is exponential rather than linear (e.g., Viero et al. 2022), or iii.) The current dataset (a single point and multiple upper limits) and/or model (modified blackbody) are insufficient to describe the dust properties. Since many studies of dust properties at high-redshift use a single FIR continuum detection and assume a dust temperature or template (e.g., Béthermin et al. 2020; Fudamoto et al. 2021; Bowler et al. 2023), more observations are required to resolve this ambiguity.

### 3.2 Molecular gas

A spectrum extracted from our combined data cube using an ellipse centred on the expected location of MACS0416\_Y1 is shown in Figure 3. It is clear that the observed spectrum (black line) shows no significant line emission. If there was indeed  $10^{10} M_\odot$  of molecular gas, then we would expect the line profile shown by the red Gaussian (peak amplitude=0.097 mJy, FWHM= 200  $\text{km s}^{-1}$ ; assuming  $\alpha_{CO} = 0.8 M_\odot (K \text{ km s}^{-1} \text{ pc}^2)^{-1}$ ), which peaks at  $< 1\sigma$ . That is, we lack the sensitivity to confirm or rule out this amount of molecular gas.

To place an upper limit on the integrated flux density, we first collapse the data cube around the expected CO(2-1) frequency, assuming a width of  $\sim 200 \text{ km s}^{-1}$  (based on  $\text{FWHM}_{[\text{OIII}]88\mu\text{m}}$ ; Tamura et al. 2019). This map (shown in the right panel of Fig. 3) has an RMS noise level of  $4.5 \text{ mJy beam}^{-1} \text{ km s}^{-1}$ , corresponding to a  $3\sigma$  upper limit on the integrated flux density of  $S\Delta\nu_{\text{CO}(2-1)} < 72 \text{ mJy km s}^{-1}$ .

Using the standard equation of Solomon et al. (1992), this results in an upper limit of:

$$M_{H_2} < (2.5 \times 10^{10} M_\odot) \frac{\alpha_{CO}}{0.8 M_\odot / (K \text{ km s}^{-1} \text{ pc}^2)} \frac{1.43}{\mu} \frac{1}{r_{21}} \frac{0.76}{f_{\text{CMB}}} \quad (1)$$

where we have assumed a starburst-like  $\alpha_{CO}$  and  $r_{21}$ , as motivated by the high [OIII] 88 $\mu\text{m}$ /[CII] 158  $\mu\text{m}$  ratio detected by Tamura et al. (2019) and Bakx et al. (2020), as well as the discovery of a likely starburst-driven dust bubble in high-resolution [OIII] 88 $\mu\text{m}$  imaging (Tamura et al. 2023). The effect of observing CO against the CMB is taken into account through the factor  $f_{\text{CMB}}$  (da Cunha et al. 2013):

$$f_{\text{CMB}} \equiv \frac{S_{\text{CO,observed}}}{S_{\text{CO,intrinsic}}} = 1 - \frac{B_\nu(T_{\text{CMB}})}{B_\nu(T_{\text{ex,CO}})} \quad (2)$$

where  $S_{\text{CO}}$  is the CO(2-1) flux density and  $B_\nu(T)$  is a blackbody function. We assume that the dust and molecular gas are in thermal equilibrium ( $T_{\text{ex,CO}} = T_D \sim 90$  K).

This dust temperature is the lower limit implied by the SED exploration of Section 3.1, and a higher  $T_D$  results in a higher  $f_{\text{CMB}}$  and thus smaller limit on  $M_{H_2}$  (e.g.,  $f_{\text{CMB}} = 0.84$  for  $T_D = 130$  K, yielding a limit of  $M_{H_2} < 2.2 \times 10^{10} M_\odot$ ). These temperatures are quite high, but a derivation of  $T_{\text{ex,CO}}$  requires multiple CO detections and excitation modelling (e.g., Daddi et al. 2015). If we assume  $T_D = 90$  K, but Milky Way-like values of  $\alpha_{CO} \sim 4.3$  and  $r_{21} \sim 0.5$  (e.g., Carilli & Walter 2013), this results in a much more conservative limit of  $M_{H_2} < 2.6 \times 10^{11} M_\odot$ .

Previous [CII] observations yielded a luminosity of  $L_{[\text{CII}]} = (1.40 \pm 0.22) \times 10^8 L_\odot$  (Bakx et al. 2020). This line has proven to be a reliable tracer of SFR in galaxies at low and high redshift (e.g., De Looze et al. 2014; Schaerer et al. 2020), although some studies have found that it acts as a reliable tracer of molecular gas (e.g., Zanella et al. 2018; Madden et al. 2020; Gurman et al. 2023). While the  $L_{[\text{CII}]}-M_{H_2}$  relation may represent a linked relation between  $L_{[\text{CII}]}$ -SFR and SFR- $M_{H_2}$  (i.e., the Kennicutt-Schmidt relation; Kennicutt 1998; Vizgan et al. 2022), it is clear that [CII] traces molecular gas that is faint in CO emission (i.e., ‘CO-dark’ gas; Hu

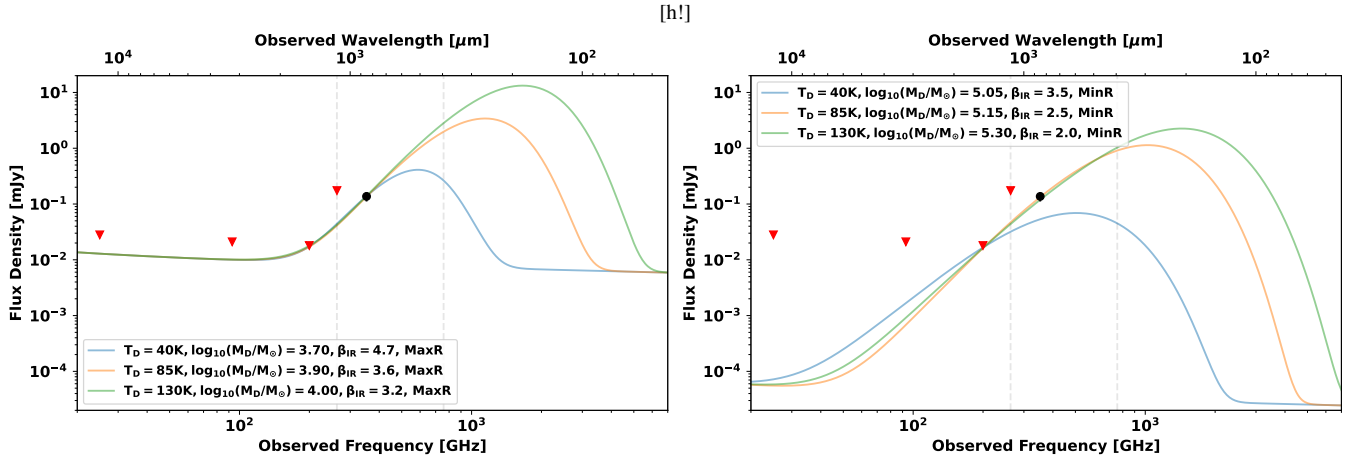


**Figure 2.** Radio-FIR SED of MACS0416\_Y1. We include our upper limit of the 25 GHz flux density, as well as a detection and limits from [Tamura et al. \(2019\)](#), [Bakx et al. \(2020\)](#), and archival data (band 3, 2021.1.00075.S; PI Ono). The detection is shown as a black circle with  $1\sigma$  error bars, while the upper limits are shown at  $3\sigma$  as downward-facing red triangles. The left panel shows the assumption of maximum non-thermal contribution, while the right panel includes the non-thermal contribution assuming  $\text{SFR} \sim 100 M_{\odot} \text{ year}^{-1}$ . In each panel, we show illustrative models that meet the detections and limits. Dashed vertical lines denote the integration range for  $L_{\text{FIR}}$  ( $\lambda_{\text{rest}} = 42.5 - 122.5 \mu\text{m}$ ).

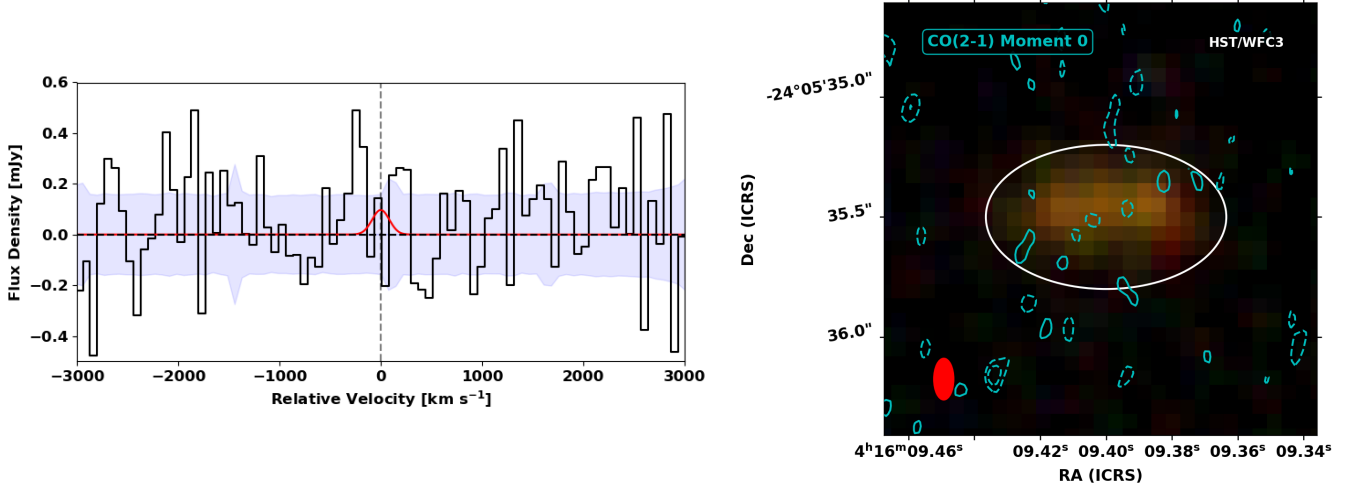


**Figure 3.** Observed CO(2-1) properties from our JVLA observations. The left panel shows a spectrum extracted from a  $1.0'' \times 0.6''$  ellipse centred on the position of MACS0416\_Y1 (black lines) with associated  $1\sigma$  uncertainty (blue shaded region). We also show the expected CO(2-1) line profile for a  $10^{10} M_{\odot}$  gaseous reservoir (red profile; assuming  $\text{FWHM} = 200 \text{ km s}^{-1}$  and  $\alpha_{\text{CO}} = 0.8$ ), which is neither confirmed nor excluded by our data. The right panel is a CO(2-1) moment 0 map for  $v = [-100, 100] \text{ km s}^{-1}$  of MACS0416\_Y1 (cyan contours), where contours are shown at  $\pm 2, 3, 4, \dots \times \sigma$  ( $1\sigma = 4.5 \text{ mJy beam}^{-1}$ ). For reference, we include a three-colour image of HST/WFC3 (F105W/F125W/F140W). The synthesised beam is represented by a filled red ellipse to the lower left, while the assumed aperture of MACS0416\_Y1 is given as a hollow white ellipse.

[et al. 2021](#)). Using  $\alpha_{[\text{CII}]} \sim 30 M_{\odot} L_{\odot}^{-1}$  ([Zanella et al. 2018](#)) results in an estimated  $M_{\text{H}_2} \sim 4.2 \times 10^9 M_{\odot}$  for MACS0416\_Y1.

We may also use the predicted dust mass of Section 3.2 ( $\sim 10^5 M_{\odot}$ ) to estimate  $M_{\text{H}_2}$  by adopting the dust-to-gas ratio ( $\delta_{\text{DGR}}$ ) prescription of [Li et al. \(2019\)](#):

$$\log_{10}(\delta_{\text{DGR}}) = (2.445 \pm 0.006) \log_{10}(Z') - (2.029 \pm 0.003) \quad (3)$$

where  $Z' = Z/Z_{\odot}$ . If we assume  $Z' \sim 0.25$  ([Bakx et al. 2020](#)), this results in  $\delta_{\text{DGR}} \sim 10^{-3.5}$ , and a predicted gas mass of  $M_{\text{H}_2} \sim 10^{8.5} M_{\odot}$ . Since this relation was derived using a sample of star-forming main sequence galaxies at  $z \sim 0 - 6$  and MACS0416\_Y1 is likely a starbursting galaxy at higher redshift, it is conceivable that MACS0416\_Y1 may feature an even smaller  $\delta_{\text{DGR}}$  value (as

seen in other high-redshift sources; e.g., [Hashimoto et al. 2023](#)), and consequently a higher  $M_{\text{H}_2}$ .

A [CII] velocity gradient was detected in this source, which was assumed to be rotation, resulting in a dynamical mass estimate of  $M_{\text{dyn}} = (1.2 \pm 0.4) \times 10^{10} M_{\odot}$  ([Bakx et al. 2020](#)). Since high-resolution [OIII] observations revealed that this source is composed of several clumps with complex kinematics, this value may only be used as an approximate estimate. However, since the stellar mass of this object is approximately  $M_{*} \sim 10^9 M_{\odot}$  ([Tamura et al. 2019](#)) and we find a small dust mass ( $M_{\text{D}} \sim 10^5 M_{\odot}$ ), there may be room in the mass budget for a large amount of gas ( $\sim 10^{10} M_{\odot}$ ).

To summarise, the [CII] luminosity of this source implies  $M_{\text{H}_2} \sim 4.2 \times 10^9 M_{\odot}$ , which is in agreement with the mass limits imposed by

Method	$M_{H_2}$ [ $M_{\odot}$ ]
$L_{CO(2-1),SB}$	$< 2.5 \times 10^{10}$
$L_{CO(2-1),MS}$	$< 2.6 \times 10^{11}$
[CII] Luminosity	$\sim 4.2 \times 10^9$
$\delta_{DGR}$	$\sim 3.1 \times 10^8$
[CII] Dynamical Decomposition	$< 1.1 \times 10^{10}$

**Table 1.** Estimates of  $M_{H_2}$  from different tracers.

the non-detection of CO(2-1) and from a dynamical mass decomposition, as well as an approximate dust-based estimate. Cosmological zoom-in simulations of galaxies at  $z \sim 6 - 7$  suggest smaller gas masses for a comparable galaxy ( $M_{H_2} \sim 10^{8.5} M_{\odot}$ , Vallini et al. 2012; Pallottini et al. 2017), while observations of more massive galaxies at  $z \sim 6 - 7$  return larger molecular gas masses (e.g., Ono et al. 2022; Feruglio et al. 2023). It can be clearly seen from the values listed in Table 1 that the available data suggest a broad mass range of  $M_{H_2} \sim 10^{8.5-11.3} M_{\odot}$ . In order to place a tighter constraint, the gas-phase metallicity is required to calibrate  $\delta_{DGR}$  and  $\alpha_{CO}$ . Luckily, upcoming JWST observations of this source with the integral field unit (IFU) of the Near-Infrared Spectrograph (NIRSpec; PID 1208, PI Willott) will target MACS0416\_Y1 in both low- ( $R \sim 100$ ; Prism) and high-spectral resolution ( $R \sim 2700$ ; G395H), which will result in a precise estimate of metallicity through well-tested rest-frame optical line ratios.

#### 4 CONCLUSION

Here, we present an updated analysis of the dust and molecular gas properties in the  $z \sim 8.31$  galaxy MACS0416\_Y1, including both archival data and new JVLA observations targeting CO(2-1) and rest-frame radio continuum emission.

Since the continuum emission is not detected at  $\nu_{obs} \sim 25$  GHz, we examine the implications this has on the non-thermal emission. Assuming a standard non-thermal fraction and synchrotron slope, our non-detection implies a 1.4 GHz upper limit of  $S_{1.4GHz} < 120 \mu Jy$ . If the Kennicutt (1998) scaling law is applied, this results in a  $SFR_{radio} \lesssim 2.5 \times 10^4 M_{\odot} \text{ year}^{-1}$ . This is much larger than the observed SFR, implying an uninformative constraint. Assuming a lower  $SFR \sim 10^2 M_{\odot} \text{ year}^{-1}$  results in  $S_{1.4GHz} \sim 0.5 \mu Jy$ , and thus a minuscule contribution of nonthermal emission to the luminosity.

The archival FIR SED (which consists of multiple non-detections and one detection) is re-examined and modelled with a modified blackbody. We find that these data suggest a low dust mass ( $\sim 10^5 M_{\odot}$ ) and high dust temperature ( $T_D \gtrsim 90$  K), in agreement with past results (Bakx et al. 2020).

Our non-detection of CO(2-1) is used to place a constraint on  $M_{H_2}$ , which is compared to estimates from [CII] luminosity, dust mass, and [CII] kinematics. While the  $L_{[CII]}$ -based estimate of the  $H_2$  mass ( $\sim 4.2 \times 10^9 M_{\odot}$ ) is in agreement with the CO-based limit ( $< 2.5 \times 10^{10} M_{\odot}$ ) and a mass decomposition based on  $M_{dyn,[CII]}$  ( $< 1.1 \times 10^{10} M_{\odot}$ ), the dust-to-gas ratio-based estimate is much lower ( $\sim 3.1 \times 10^8 M_{\odot}$ ). If the [CII]-based estimate is accurate, this suggests a higher gas-to-dust ratio than previously expected.

While the constraints in this work are not yet precise, they will be refined greatly in the near future through synergy with high-resolution ALMA [CII], [CI], and CO observations as well as JWST/NIRSpec IFU observations (Wistok et al. in prep). These will result in new estimates of the gas-phase metallicity, non-thermal and FIR continuum emission, SFR, and gas properties in MACS0416\_Y1, enabling a detailed view of this primordial galaxy.

#### DATA AVAILABILITY

The uncalibrated datasets analysed in this work are available from the NRAO data archive (<https://data.nrao.edu/portal/#/myDataViewer>) and ALMA data archive (<https://almascience.nrao.edu/asax/>). Calibrated data are available from the corresponding author upon reasonable request.

#### ACKNOWLEDGEMENTS

GCJ acknowledges funding from the ‘‘FirstGalaxies’’ Advanced Grant from the European Research Council (ERC) under the European Union’s Horizon 2020 research and innovation programme (Grant agreement No. 789056). JW gratefully acknowledges support from the Fondation MERAC, the Science and Technology Facilities Council (STFC), the European Research Council (ERC) through Advanced Grant 695671 (‘‘QUENCH’’), and the UK Research and Innovation (UKRI) Frontier Research grant RISEandFALL. NL acknowledges support from the Kavli foundation. This paper utilizes data obtained with the ALMA Observatory, under program 2021.1.00075.S. ALMA is a partnership of ESO (representing its member states), NSF (USA) and NINS (Japan), together with NRC (Canada), MOST and ASIAA (Taiwan), and KASI (Republic of Korea), in cooperation with the Republic of Chile. We thank the anonymous reviewer for constructive feedback that strengthened this work.

#### REFERENCES

- Algera H. S. B., et al., 2021, *ApJ*, 912, 73  
 Aravena M., et al., 2023, *arXiv e-prints*, p. arXiv:2309.15948  
 Bakx T. J. L. C., et al., 2020, *MNRAS*, 493, 4294  
 Bakx T. J. L. C., et al., 2021, *MNRAS*, 508, L58  
 Beelen A., Cox P., Benford D. J., Dowell C. D., Kovács A., Bertoldi F., Omont A., Carilli C. L., 2006, *ApJ*, 642, 694  
 Béthermin M., et al., 2020, *A&A*, 643, A2  
 Bolatto A. D., Wolfire M., Leroy A. K., 2013, *ARA&A*, 51, 207  
 Boogaard L. A., et al., 2023, *ApJ*, 945, 111  
 Bouwens R., et al., 2020, *ApJ*, 902, 112  
 Bowler R. A. A., et al., 2023, *arXiv e-prints*, p. arXiv:2309.17386  
 Brammer G. B., et al., 2016, *ApJS*, 226, 6  
 Brinchmann J., Charlot S., Kauffmann G., Heckman T., White S. D. M., Tremonti C., 2013, *MNRAS*, 432, 2112  
 CASA Team et al., 2022, *PASP*, 134, 114501  
 Carilli C. L., Walter F., 2013, *ARA&A*, 51, 105  
 Carniani S., et al., 2019, *MNRAS*, 489, 3939  
 Concas A., Popesso P., 2019, *MNRAS*, 486, L91  
 Condon J. J., 1992, *ARA&A*, 30, 575  
 D’Odorico V., et al., 2018, *ApJ*, 863, L29  
 D’Silva J. C. J., Lagos C. D. P., Davies L. J. M., Lovell C. C., Vijayan A. P., 2023, *MNRAS*, 518, 456  
 Daddi E., et al., 2015, *A&A*, 577, A46  
 De Looze I., et al., 2014, *A&A*, 568, A62  
 Decarli R., et al., 2019, *ApJ*, 882, 138  
 Decarli R., et al., 2022, *A&A*, 662, A60  
 Decarli R., et al., 2023, *A&A*, 673, A157  
 Eales S., Gomez H., Dunne L., Dye S., Smith M. W. L., 2023, *arXiv e-prints*, p. arXiv:2303.07376  
 Feruglio C., et al., 2023, *ApJ*, 954, L10  
 Frias Castillo M., et al., 2023, *ApJ*, 945, 128  
 Fudamoto Y., et al., 2021, *Nature*, 597, 489  
 García-Vergara C., et al., 2022, *ApJ*, 927, 65  
 Gurman A., Hu C.-Y., Sternberg A., van Dishoeck E. F., 2023, *arXiv e-prints*, p. arXiv:2308.07338  
 Güver T., Özel F., 2009, *MNRAS*, 400, 2050

- Hashimoto T., et al., 2023, *ApJ*, 952, 48
- Hodge J. A., Carilli C. L., Walter F., de Blok W. J. G., Riechers D., Daddi E., Lentati L., 2012, *ApJ*, 760, 11
- Hu C.-Y., Sternberg A., van Dishoeck E. F., 2021, *ApJ*, 920, 44
- Ikarashi S., Ivison R. J., Cowley W. I., Kohno K., 2022, *A&A*, 659, A154
- Jarugula S., et al., 2021, *ApJ*, 921, 97
- Jiménez-Andrade E. F., et al., 2018, *A&A*, 615, A25
- Jones G. T., Stanway E. R., 2023, *MNRAS*, 525, 5720
- Jones G. C., Maiolino R., Caselli P., Carniani S., 2020, *MNRAS*, 498, 4109
- Kawamata R., Oguri M., Ishigaki M., Shimasaku K., Ouchi M., 2016, *ApJ*, 819, 114
- Kennicutt Robert C. J., 1998, *ApJ*, 498, 541
- Laporte N., et al., 2015, *A&A*, 575, A92
- Lee K., et al., 2023, *ApJ*, 944, 35
- Li Q., Narayanan D., Davé R., 2019, *MNRAS*, 490, 1425
- Liang L., et al., 2019, *MNRAS*, 489, 1397
- Madden S. C., et al., 2020, *A&A*, 643, A141
- Manning S. M., et al., 2022, *ApJ*, 925, 23
- Mitsuhashi I., et al., 2023, *arXiv e-prints*, p. arXiv:2311.16857
- Narayanan D., Krumholz M. R., Ostriker E. C., Hernquist L., 2012, *MNRAS*, 421, 3127
- Ono Y., et al., 2022, *ApJ*, 941, 74
- Pallottini A., Ferrara A., Gallerani S., Vallini L., Maiolino R., Salvadori S., 2017, *MNRAS*, 465, 2540
- Pavesi R., et al., 2018, *ApJ*, 861, 43
- Pavesi R., Riechers D. A., Faisst A. L., Stacey G. J., Capak P. L., 2019, *ApJ*, 882, 168
- Popesso P., et al., 2023, *MNRAS*, 519, 1526
- Riechers D. A., et al., 2006, *ApJ*, 650, 604
- Riechers D. A., et al., 2021a, *ApJ*, 907, 62
- Riechers D. A., Cooray A., Pérez-Fournon I., Neri R., 2021b, *ApJ*, 913, 141
- Schaerer D., et al., 2020, *A&A*, 643, A3
- Scoville N., et al., 2016, *ApJ*, 820, 83
- Solomon P. M., Downes D., Radford S. J. E., 1992, *ApJ*, 398, L29
- Speagle J. S., Steinhardt C. L., Capak P. L., Silverman J. D., 2014, *ApJS*, 214, 15
- Stanley F., et al., 2023, *ApJ*, 945, 24
- Tamura Y., et al., 2019, *ApJ*, 874, 27
- Tamura Y., et al., 2023, *ApJ*, 952, 9
- Vallini L., Dayal P., Ferrara A., 2012, *MNRAS*, 421, 3266
- Vieira D., Riechers D. A., Pavesi R., Faisst A. L., Schinnerer E., Scoville N. Z., Stacey G. J., 2022, *ApJ*, 925, 174
- Viero M. P., Sun G., Chung D. T., Moncelsi L., Condon S. S., 2022, *MNRAS*, 516, L30
- Vizgan D., et al., 2022, *ApJ*, 929, 92
- Walter F., Weiß A., Downes D., Decarli R., Henkel C., 2011, *ApJ*, 730, 18
- Witstok J., Jones G. C., Maiolino R., Smit R., Schneider R., 2023, *MNRAS*, 523, 3119
- Zanella A., et al., 2018, *MNRAS*, 481, 1976
- Zavala J. A., 2021, *Research Notes of the American Astronomical Society*, 5, 15
- da Cunha E., et al., 2013, *ApJ*, 766, 13